

Chern-Textured Exciton Insulators with Valley Spiral Order in Moiré Materials

Ziwei Wang,^{1,*} Yves H. Kwan,^{2,*} Glenn Wagner,³ Steven H. Simon,¹ Nick Bultinck,⁴ and S.A. Parameswaran¹

¹*Rudolf Peierls Centre for Theoretical Physics, Parks Road, Oxford, OX1 3PU, UK*

²*Princeton Center for Theoretical Science, Princeton University, Princeton NJ 08544, USA*

³*Department of Physics, University of Zurich, Winterthurerstrasse 190, 8057 Zurich, Switzerland*

⁴*Department of Physics, Ghent University, Krijgslaan 281, 9000 Gent, Belgium*

We explore the phase diagrams of moiré materials in search of a new class of intervalley-coherent correlated insulating state: the Chern texture insulator (CTI). This phase of matter, proposed in a companion paper [1], breaks valley $U(1)$ symmetry in a nontrivial fashion wherein the valley order parameter is forced to texture in momentum space as a consequence of band topology. Using detailed Hartree-Fock studies, we establish that the CTI emerges as an energetically competitive intermediate-coupling ground state in several moiré systems which lack a twofold rotation symmetry that forbids the single-particle topology essential to the formation of the CTI valley texture.

I. INTRODUCTION

Moiré materials — heterostructures of layered atomically-thin constituents stacked with a lattice or rotational mismatch — have ushered in a new paradigm of correlated electronic matter with unprecedented tunability and diversity. Experiments in recent years have uncovered a rich variety of strongly-interacting phenomena including superconductivity [2–5], correlated insulators [3, 4, 6], orbital ferromagnetism [7, 8], (fractional) Chern insulators [9–14], linear- T resistivity [15, 16], generalized Wigner crystals [17], and many others. The pioneering studies focused on magic-angle twisted bilayer graphene (TBG), but an ever-growing research effort has been invested into other systems involving larger numbers of layers [18, 19] and alternative material building blocks [20]. While different moiré platforms can vary significantly in the details of their single-particle models and hence interacting phenomenology, they often share several fundamental features. Firstly, the region in parameter space of greatest interest is typically where some subset of the bands are isolated and narrow, and electronic interactions can be expected to play a non-trivial role. Secondly, most moiré materials carry flavor degrees of freedom such as spin and valley, which can participate in symmetry-breaking phenomena. Finally, the low-energy moiré bands are often topologically non-trivial.

The confluence of these three features have motivated parallels to an older problem: namely, that of quantum Hall ferromagnetism (QHFM) [21]. This is usually exhibited by electrons with flavor degrees of freedom in exactly-flat bands characterized by a topological Chern number $C = 1$: the celebrated Landau levels of electrons in a magnetic field. A direct analogy between the two problems is complicated by two facts. The first is that single-particle moiré bands intrinsically preserve time-reversal symmetry (\hat{T}), whose breaking is a prerequisite for $C \neq 0$. This means that the bands either (i) do not have a readily definable Chern number (as is the case, for

instance, when they are endowed with an additional \hat{C}_{2z} spatial rotation symmetry, leading to a distinct ‘Euler invariant’ topological index); or else (ii) come in time-reversed partners with equal and opposite Chern numbers. The second is that moiré bands are never exactly flat, and moreover interactions can feed back nontrivially on their dispersion, potentially modifying the balance of interaction and kinetic energy. Together, these open the possibility for new phases of matter unanticipated from the strong-coupling, QHFM-like limit.

Pursuing this line of inquiry, in a companion work [1] we introduced a new class of broken-symmetry topological phase that we termed the “textured exciton insulator” (TEI), as a candidate ground state for moiré materials whose single-particle bands are topological and carry a conserved $U(1)_V$ ‘valley’ charge. Here the excitonic order parameter introduces intervalley coherence, thereby spontaneously breaks $U(1)_V$, and is forced to ‘texture’ across the Brillouin zone due to the mandates of band topology [22]. We established several universal aspects of TEIs linked to their intertwining of symmetry-breaking and topology, including identifying a topological obstruction to giving them a local-moment description [1].

TEIs come in two varieties, depending on the two classes of time-reversal-invariant bandstructure structure discussed above. The first, the “Euler texture insulator” (ETI) is linked to $\hat{C}_{2z}\hat{T}$ -invariant bands with a nonzero Euler index in each valley [23, 24], whereas the second, the “Chern texture insulator” emerges in \hat{C}_{2z} -broken systems with valley-contrasting Chern numbers. Using general arguments and simplified toy models, we demonstrated in Ref. [1] that TEIs are energetically competitive ground states at intermediate coupling at some partial (integer) filling of the bands. In the ETI case, we further identified the incommensurate Kekulé spiral (IKS) phase predicted [25], and subsequently observed [26, 27] in magic-angle bi/tri-layer [28] graphene as an ETI. Given that this establishes the ETI as an experimentally-relevant concept, this naturally stimulates a search for its Chern-textured counterpart in other systems.

With this motivation, here we explore the phase diagrams of different moiré materials that break \hat{C}_{2z} ei-

* These authors contributed equally.

System	\hat{C}_{2z} -breaking	CTI $_n$ index	Phase Diag.
TDBG (ABAB)	explicit	2	Fig. 2
TDBG (ABBA)	explicit	0, 1, -1	Figs. 4,5
TMBG	explicit	0, 2	Fig. 7
HTG	explicit	0, 1	Fig. 8
$t\text{MoTe}_2$	explicit	0	Fig. 9b
TSTG	spontaneous	0	Fig. 10b

TABLE I. **Chern-textured exciton insulators (CTIs) in moiré materials studied in this work.** The IVC order parameter winding is $4\pi n$ in the CTI $_n$ phase. For $n = 0$, the state is considered a ‘trivial IVC’ phase. [$t\text{MoTe}_2$: twisted bilayer MoTe_2 ; TDBG: twisted double-bilayer graphene; TMBG: twisted mono-bilayer graphene; HTG: helical trilayer graphene; TSTG: twisted symmetric trilayer graphene; TBG: twisted bilayer graphene].

ther explicitly or spontaneously. Using microscopically faithful self-consistent Hartree-Fock (HF) calculations, we demonstrate that CTIs are energetically competitive ground states in many of these materials. En route, we address the various further complications of realistic materials absent in simplified models, such as various competing orders, the interaction-induced hybridization of single-particle bands within each valley, etc. Even after incorporating these features, we find robust CTI order survives within a reasonable parameter regime across a large class of materials, as summarized in Tab. I. In each of these cases, the order is linked to a moiré-scale modulation of intervalley coherence, that in several cases can potentially be directly detected through scanning probe measurements similar to those used to identify IKS order [26, 27]. Our work thus provides yet another illustration of how the combinatorial versatility of moiré systems provides fertile ground for seeking new and complex correlated states of matter with cutting-edge probes.

The remainder of this paper is organized as follows. In Sec. II, briefly summarize the theory of the CTI, summarize the single-particle continuum models of the moiré materials considered in this paper, and discuss details of the HF calculations. We present the results of our numerical studies in the form of HF phase diagrams for each of the materials summarized in Tab. I in Sec. III, and close with a final discussion in Sec. IV.

II. BACKGROUND, MODELS, AND METHODS

A. Chern Texture Insulators

The simplest setting in which a CTI can arise consists of a pair of Chern bands with Chern number $C_\tau = \tau n$, distinguished by a time-reversal-odd ‘valley’ index $\tau = \pm 1$. The interacting Hamiltonian has time-reversal symmetry (TRS) \hat{T} , which relates the two valleys, and $U_V(1)$ symmetry, i.e. the independent conservation of

charge in each valley. In all the cases we study, the spin structure is such that we can choose implementation of time reversal to satisfy $\hat{T}^2 = +1$. The absence of a valley-exchanging \hat{C}_{2z} symmetry, whether due to explicit single-particle symmetry-breaking effects or interaction driven spontaneous symmetry breaking, is therefore crucial for allowing a non-zero valley Chern number¹. In the limit where interactions dominate the kinetic energy, the ground state of the system at half-filling is expected to be a valley-polarized Chern insulator that breaks TRS [22, 29, 30]. In the intermediate-coupling regime where the kinetic energy is of similar magnitude as the interaction scale, we argued in Ref. 1 that a time-reversal-symmetric intervalley coherent insulator, which spontaneously breaks the $U_v(1)$ symmetry, is a generically competitive ground state. Due to the different Chern numbers in the two valleys, the intervalley coherence (IVC) acquires a $4\pi C$ winding around the Brillouin zone (BZ), which forces its vanishing at vortices within the Brillouin zone. In order to open an insulating gap, the valley pseudospin forms a complex texture in the BZ and fully valley polarizes at the cores of the IVC vortices. The resulting state is a Chern texture insulator denoted CTI $_n$, where the additional index n indicates the Chern number of the underlying valley-diagonal bands $C = \pm n$ (and hence fixes the enforced winding of the IVC order in the BZ to be $4\pi n$). We demonstrated that the CTI exhibits a form of delicate topology in an obstruction to an atomically-localized limit. One further complication is that, in general, it is possible for IVC to develop between Bloch states with momentum \mathbf{k} in valley $\tau = +$ and momentum $\mathbf{k} + \mathbf{q}$ in valley $\tau = -$, with \mathbf{q} the wavevector of the resulting intervalley spiral order. The value of \mathbf{q} realized in the ground state depends on the kinetic energy landscape of the system. We note that there exists a \mathcal{T} -breaking cousin of the CTI which also exhibits a winding IVC across the BZ, but where the IVC vortex cores have the *same sense* of VP. This ‘tilted valley polarized’ (TVP) phase has nonzero Chern number, yet is distinct on grounds of both symmetry and topology from the fully-VP state, and is often found proximate to the CTI in the phase diagram of the toy models we have explored. Readers interested in details of the CTI and TVP and their topological properties beyond this brief account are directed to the companion paper, Ref. [1].

B. Continuum Models

We perform self-consistent HF calculations on several moiré materials. To do so, we adopt the approach of first modeling the non-interacting moiré band structure within the ‘continuum model’ approximation [31]

¹ This should be contrasted against the ETI setting, where single-valley $\hat{C}_{2z}\hat{T}$ symmetry is essential [1].

4. Helical trilayer graphene

Helical trilayer graphene (HTG) is a supermoiré material that consists of three layers of graphene that are rotated consecutively with identical twist angles θ . While HTG preserves \hat{C}_{2z} on the global scale, relaxation calculations show that it relaxes into large moiré-periodic domains (referred to as h-HTG and \bar{h} -HTG) of linear dimension ~ 100 nm (near the magic angle $\theta \sim 1.8^\circ$), that individually break \hat{C}_{2z} and are mapped into each other under \hat{C}_{2z} [58–60]. The interacting physics of HTG can then be understood by focusing on the properties of the individual domains.

We closely follow the conventions of Ref. [61]. Considering valley K and h-HTG without loss of generality, the continuum Hamiltonian is $H_K = H_{K,0} + H_V$, where

$$H_{K,0} = \begin{pmatrix} -iv_F \boldsymbol{\sigma} \cdot \nabla & T(\mathbf{r} - \mathbf{d}_t) & 0 \\ T^\dagger(\mathbf{r} - \mathbf{d}_t) & -iv_F \boldsymbol{\sigma} \cdot \nabla & T(\mathbf{r} - \mathbf{d}_b) \\ 0 & T^\dagger(\mathbf{r} - \mathbf{d}_b) & -iv_F \boldsymbol{\sigma} \cdot \nabla \end{pmatrix} \quad (11)$$

with $v_F = 8.8 \times 10^5 \text{ ms}^{-1}$, and $H_V = \text{diag}(-1/2, 0, 1/2)\Delta V$. Note that the wavefunction in each layer is written relative to its Dirac point (this is very slightly strained to accommodate a moiré periodicity), and as a consequence the relevant interlayer tunneling are shifted by $\mathbf{d}_{t,b}$ in the top and bottom layer. The unshifted tunneling matrix is given by³

$$T(\mathbf{r}) = \begin{pmatrix} w_{AA}t_0(\mathbf{r}) & w_{AB}t_{-1}(\mathbf{r}) \\ w_{AB}t_1(\mathbf{r}) & w_{AA}t_0(\mathbf{r}) \end{pmatrix} \quad (12)$$

$$t_\alpha(\mathbf{r}) = \sum_{n=0}^2 e^{\frac{2\pi i}{3}n\alpha} e^{-i\mathbf{q}_n \cdot \mathbf{r}}$$

$$q_{n,x} + iq_{n,y} = -ik_\theta e^{\frac{2\pi i}{3}n},$$

where $\mathbf{K}_{1,3} = \mp \mathbf{q}_0 + \mathbf{K}_2$. We use $w_{AA} = 75 \text{ meV}$ and $w_{AB} = 110 \text{ meV}$. The relative shifts of the layers in h-HTG are parameterized by $\mathbf{d}_t - \mathbf{d}_b = \boldsymbol{\delta} = \frac{1}{3}(\mathbf{a}_2 - \mathbf{a}_1)$, where $\mathbf{a}_{1,2} = \frac{4\pi}{3k_\theta}(\pm \frac{\sqrt{3}}{2}, \frac{1}{2})$.

5. Twisted homobilayer MoTe₂

We closely follow the conventions of Refs. [62, 63] in our description of the continuum model [64] for the valence bands of AA-stacked homobilayer MoTe₂ with small twist angle ($t\text{MoTe}_2$). This system also lacks \hat{C}_{2z} , and due to strong spin-orbit coupling, the valence bands are spin-valley locked such that $\tau = +$ ($\tau = -$) is tied to spin- \uparrow (spin- \downarrow). In valley K , the rotated K -point of the top layer is at $\mathbf{K}_t = \frac{4\pi}{3a_0}(\cos \theta/2, -\sin \theta/2)$, while that of

the bottom layer is at $\mathbf{K}_b = \frac{4\pi}{3a_0}(\cos \theta/2, \sin \theta/2)$, where $a_0 = 0.352 \text{ nm}$ is the lattice constant. In terms of $\mathbf{q}_1 = \mathbf{K}_b - \mathbf{K}_t$, we have the basis moiré RLVs $\mathbf{b}_1 = (\hat{C}_3^2 - \hat{C}_3)\mathbf{q}_1$ and $\mathbf{b}_2 = -\hat{C}_3^2\mathbf{b}_1$, where \hat{C}_3 is a counterclockwise rotation by $2\pi/3$.

In layer space, the real-space continuum Hamiltonian takes the form

$$H_K = \begin{pmatrix} h_{\tau,b}(\mathbf{r}) & t_\tau(\mathbf{r}) \\ t_\tau^*(\mathbf{r}) & h_{\tau,t}(\mathbf{r}) \end{pmatrix}. \quad (13)$$

The intralayer term (in a layer-dependent frame centered at the corresponding Dirac momentum) is

$$h_{\tau,l}(\mathbf{r}) = \frac{\hbar^2 \nabla^2}{2m^*} + V_{\tau,l}(\mathbf{r}) + (-1)^l \frac{\Delta V}{2}, \quad (14)$$

where m^* is the effective mass. The intralayer moiré potential $V_{\tau,l}(\mathbf{r})$ and interlayer hopping $t_\tau(\mathbf{r})$ are, at the first harmonic level, given by

$$V_{\tau,l}(\mathbf{r}) = V e^{-(-1)^l i\psi} \sum_{i=1,2,3} e^{i\mathbf{g}_i \cdot \mathbf{r}} + \text{c.c.} \quad (15)$$

$$t_\tau(\mathbf{r}) = w \sum_{i=1,2,3} e^{-i\tau \mathbf{q}_i \cdot \mathbf{r}}, \quad (16)$$

where $(-1)^t = 1$ and $(-1)^b = -1$, and $\mathbf{g}_i = \hat{C}_3^{i-1}\mathbf{b}_1$.

In the main text, we focus on twist angles $\theta = 3.4^\circ - 4.0^\circ$, and use the parameters of Ref. [65], i.e. $m^* = 0.6m_e$, $w = -23.8 \text{ meV}$, $V = 20.8 \text{ meV}$, $\psi = -107.7^\circ$. We have also checked that our conclusions on the nature of the IVC state remain unchanged using the parameters of Ref. [66], i.e. $m^* = 0.62m_e$, $w = -13.3 \text{ meV}$, $V = 11.2 \text{ meV}$, $\psi = -91^\circ$. However, we have not exhaustively explored the extended parameter space of the relevant models in full, leaving this as a subject for future work.

6. Twisted symmetric trilayer graphene

Twisted symmetric trilayer graphene (TSTG) [5, 19, 27, 67–76] is a \hat{C}_{2z} -symmetric heterostructure that consists of three sheets of monolayer graphene stacked together, with the middle layer twisted by θ relative to the top and bottom layers. Using the conventions established in Sec. II B 1, the single-particle Hamiltonian for TSTG in valley K is given by [77–79]

$$H_K = \begin{pmatrix} H_0(\mathbf{k}_1) - \frac{1}{2}\Delta V & U & \\ U^\dagger & H_0(\mathbf{k}_2) & U^\dagger \\ & U & H_0(\mathbf{k}_1) + \frac{1}{2}\Delta V \end{pmatrix}. \quad (17)$$

We use $w_{AB} = 0.11 \text{ eV}$, $w_{AA} = 0.075 \text{ eV}$, $\gamma_0 = 2.73 \text{ eV}$ (which defines the graphene Fermi velocity as $v = \frac{3a}{2\hbar}\gamma_0$) and twist angle $\theta = 1.56^\circ$.

C. Details of Hartree-Fock calculations

We will be interested in electronic filling factors ν near charge neutrality, which corresponds to $\nu = 0$. Since

³ The interlayer tunneling here does not include effects of the momentum-dependence of the tunneling [58]. See App. A 1 for a discussion of this correction.

interaction-induced phenomena primarily involve just a few low energy moiré bands, which are often energetically separated from higher ‘remote’ bands, we project our calculations into a subset of ‘active’ bands. These are associated with band creation operators $c_{\mathbf{k},f,a}^\dagger$, where \mathbf{k} is a momentum in the moiré BZ (mBZ), f is a spin-valley flavor index, and a is a band index. For both variants of TDBG, TMBG, and h-HTG, we take the active bands to be the central two moiré bands per spin and valley. For $t\text{MoTe}_2$, we project onto the highest three valence bands per valley. For TSTG, we project onto the central four bands per spin and valley.

For the interaction part of the Hamiltonian, we include density-density interactions with gate-screened Coulomb potential $V(q) = (e^2/2\epsilon_0\epsilon_r q) \tanh qd_{\text{sc}}$, where d_{sc} is the screening length. For both variants of TDBG, TMBG, h-HTG, and TSTG, we use $d_{\text{sc}} = 25$ nm. For $t\text{MoTe}_2$, we use $d_{\text{sc}} = 10$ nm. To capture the uncertainty in the interaction strength, we take the relative permittivity ϵ_r to be a variable parameter.

To avoid double-counting interactions, when writing down the quartic Coulomb coupling we normal order with respect to a background or reference density matrix P^{ref} , that describes the ‘vacuum’ state around which we measure charge fluctuations. For both variants of TDBG, TMBG, and h-HTG, P^{ref} consists of occupied remote valence bands, and occupation of 1/2 within the active central bands (this is an example of the so-called ‘average’ scheme). For $t\text{MoTe}_2$, the reference density matrix corresponds to filling the valence bands to charge neutrality. For TSTG, the two central bands have occupation 1/2 and the remote valence bands are occupied in P^{ref} .

We address the resulting interacting problem using self-consistent Hartree-Fock (HF) mean field simulations. These have been shown to be a versatile and reliable tool for addressing the physics of moiré materials at or near integer fillings. The effectiveness of HF can be motivated in part from strong coupling [80–82], where for example in the case of TBG it is possible to show that it is exact in certain specialized limits in which the ground states are exact Slater determinants. Indeed, in cases where has been possible to compare against alternative beyond-mean field approaches such as exact diagonalization or density-matrix renormalization group (DMRG), these have often shown good agreement with the HF, which is numerically far less costly for a given system size. For example, DMRG studies of strained TBG at integer filling $\nu = -3$ [83] find IKS order whose properties are consistent with those of the mean-field state originally identified using HF in Ref. 25.

For the graphene-based moiré materials, we restrict to spin-collinear calculations, i.e. we constrain the density matrix $P_{f,a;f',b}(\mathbf{k}, \mathbf{k}') = \langle c_{\mathbf{k},f,a}^\dagger c_{\mathbf{k}',f',b} \rangle$ to be diagonal in spin. Since we are interested in valley spirals, we enforce a generalized translation invariance parameterized by a boost wavevector \mathbf{q} . This means that IVC is only permitted at wavevector \mathbf{q} , such that \mathbf{k} in valley $\tau = +$ hybridizes with $\mathbf{k} + \mathbf{q}$ in valley $\tau = -$, leading to an

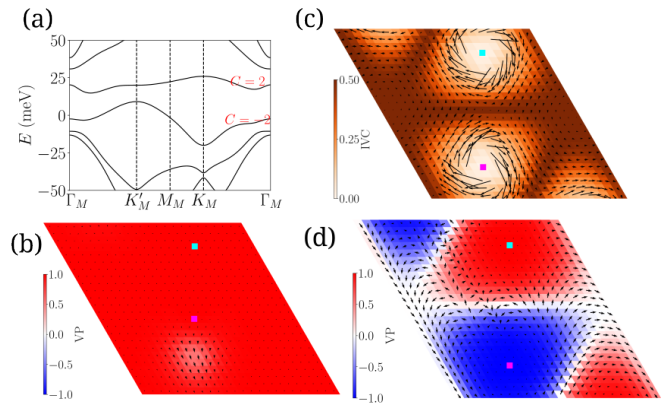


FIG. 1. **ABAB-stacked twisted double-bilayer graphene (TDBG) at $\theta = 1.2^\circ$.** a) Single-particle band structure at $\Delta V = 40$ meV in valley K ($\tau = +$). b) Momentum-dependent valley polarization (VP), shown as color, and intervalley coherence (IVC), shown with arrows, of the $\nu = +2$ tilted valley polarized (TVP) state at $\Delta V = 40$ meV and $\epsilon_r = 17$, from 24×24 HF. Cyan (magenta) square denotes Γ_M point of valley K (K'). We also note that TVP has incommensurate \mathbf{q} , as the minimum of the non-interacting conduction band is not at a high-symmetry momentum. c) The IVC intensity, shown as color, and gauge-invariant velocity (Eq. 19), shown with arrows, of the $\nu = +2$ CTI₂ at $\Delta V = 40$ meV and $\epsilon_r = 20$, from 24×24 HF. Diverging velocities very close to vortex cores are not shown. d) Same as b) except for the CTI₂ shown in c). We observe that the intervalley order winds by 8π around the mBZ, which is consistent with the Chern number difference of 4 between the conduction band in the K and K' valleys. For b,c,d), we only show the quantities in one spin sector.

intervalley spiral. On the other hand, valley-diagonal observables yield moiré translation-invariant expectation values. We perform calculations over a range of \mathbf{q} , and select the HF solution with the lowest energy. For both variants of TDBG and TMBG, we sweep over all values of \mathbf{q} on the momentum grid. For all other materials, we restrict to \hat{C}_{3z} -symmetric boosts $\mathbf{q} = \Gamma_M, K_M, K'_M$ for simplicity.

III. RESULTS

A. Twisted double-bilayer graphene (ABAB)

As shown in Fig. 1a, the single particle band structure of TDBG with ABAB stacking order at $\theta = 1.2^\circ$ has well-isolated Chern bands with $|C| = 2$ under moderate interlayer potential ΔV [44, 45, 84]. Within this window of ΔV , self-consistent HF calculations at $\nu = 1, 2, 3$ find flavor-polarized strong-coupling insulators at strong interaction strengths (i.e. small relative permittivity ϵ_r), as shown in Fig. 2. For weaker interactions, we find a greater tendency towards gapless metallic phases. However for all the fillings investigated here, we obtain insulating CTIs for a window of finite interlayer potentials.

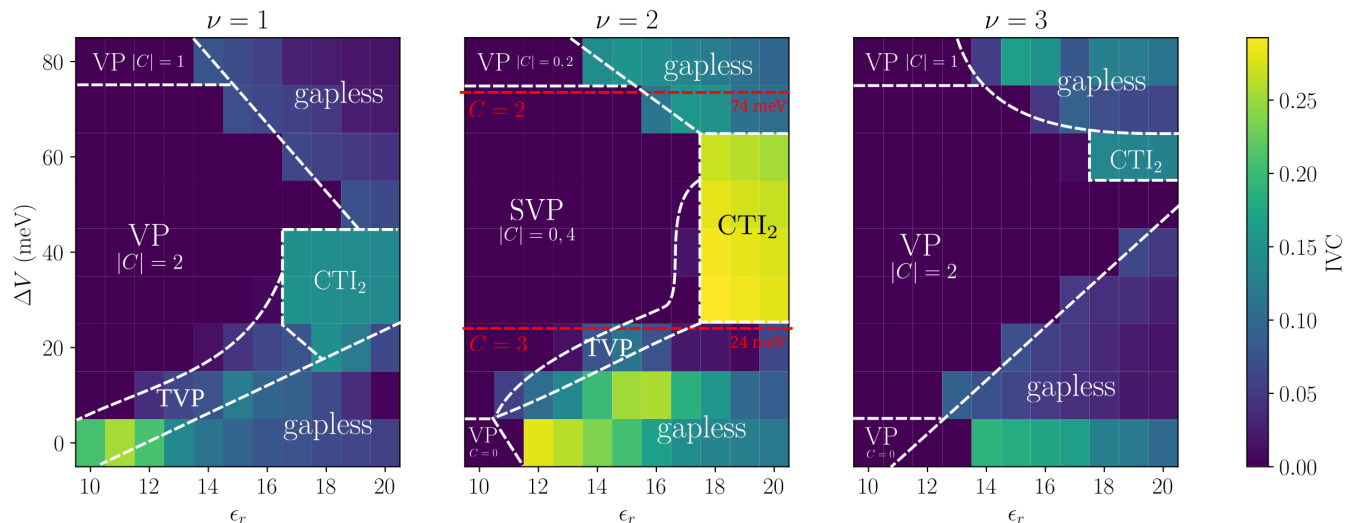


FIG. 2. **Phase diagram of ABAB-stacked twisted double-bilayer graphene (TDBG) at $\theta = 1.2^\circ$.** The results are obtained using 12×12 HF at $\nu = 1, 2, 3$. VP denotes valley-polarized states, which also carry a non-zero spin polarization. SVP denotes spin- or valley-polarized states, which are degenerate in HF. TVP denotes tilted valley-polarized states. Topological transitions in the non-interacting band structure are marked in red, with the Chern number labels that of the central conduction band.

We now focus on $\nu = 2$, where the CTI is observed over a large region of parameter space. The behaviour of the CTI at $\nu = 2$ is identical in both spin sectors, so we only show results for one spin sector. With electron doping and well-separated conduction and valence bands, we expect the non-trivial physics to occur within the non-interacting conduction bands. As such, we define the IVC order parameter $\Delta_q(\mathbf{k})$ as

$$\Delta_q(\mathbf{k}) \equiv \langle c_{\mathbf{k},+}^\dagger c_{\mathbf{k}+\mathbf{q},-} \rangle \quad (18)$$

where $c_{\mathbf{k}\tau}^\dagger$ is the spin-up electron creation operator in the conduction band of valley τ . The order parameter, shown in Fig. 1d, shows vortices with 8π -winding around the moiré Brillouin zone (mBZ), which is topologically required due to the Chern numbers $C = \pm 2$ of the constituent conduction bands. This leads us to identify the phase as a CTI_2 . We note that the vorticity is carried by two vortices with winding number 2. While the order parameter is dependent on the gauge choice⁴, we also define the gauge-independent velocity as

$$\mathbf{j}_{\mathbf{k}} = \nabla \theta_{\mathbf{k}} + \mathbf{A}_{\mathbf{k},+} - \mathbf{A}_{\mathbf{k}+\mathbf{q},-} \quad (19)$$

where $\theta_{\mathbf{k}} = \arg(\Delta_q(\mathbf{k}))$ is the angle of the IVC order parameter and $\mathbf{A}_{\mathbf{k}\tau} = i \langle u_{\mathbf{k}\tau} | \partial_{\mathbf{k}} u_{\mathbf{k}\tau} \rangle$ is the Berry-connection. As shown in Fig. 1c, the velocity diverges near the vortices, which is compensated by the vanishing IVC order parameter. In addition to the CTI_2 , we have

also found a sliver of the tilted valley-polarized (TVP) phase (Fig. 1b), which was introduced in Ref. [1].

The physics of CTI in $\nu = 1, 3$ is essentially identical to that in $\nu = 2$, except that for these odd integer fillings, IVC is only present in one of the two spin sectors (namely, the spin sector with filling factor 1 relative to its charge neutrality). We note that the interaction-induced band normalization depends on the total filling, leading to the CTI being found at different regions of parameter space for different fillings.

B. Twisted double-bilayer graphene (ABBA)

Similar to ABAB-stacked TDBG, we observe the presence of CTIs at all of $\nu = 1, 2, 3$ for ABBA-stacked TDBG (Fig. 4). We again focus on $\nu = +2$, which contains the largest region of gapped IVC insulators. However, we observe some complications not present in the simplest setting with just one band per valley. As discussed in the previous subsection, in the regime where the CTI is observed in $\nu = +2$ ABAB-stacked TDBG, the conduction band is sufficiently separated from the valence band and other remote bands to prevent them from participating non-trivially in the IVC. In ABBA-stacked TDBG, at a small interlayer potential of $\Delta V = 20$ meV, the central conduction bands are also topological with $|C| = 2$ [44, 45], but they can significantly mix with the central valence bands owing to the lack of clear energetic separation (Fig. 3a).

To understand the nature of intervalley coherent phases obtained in HF calculations in such cases, we consider the following valley-filtered basis. If the HF

⁴ App. B1 details how we implement a smooth but non-periodic gauge-fixing.

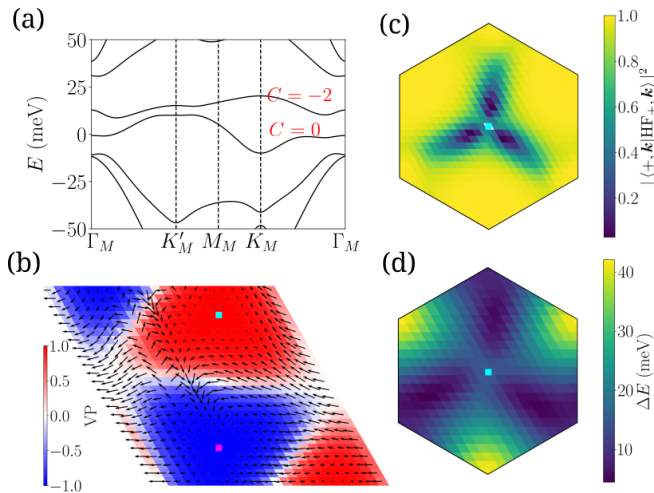


FIG. 3. **ABBA-stacked twisted double-bilayer graphene (TDBG) at $\theta = 1.2^\circ$.** a) Single-particle band structure at $\Delta V = 20$ meV in valley K ($\tau = +$). The two central bands are separated by a direct gap, making the Chern number well-defined for each band, but they have a negative indirect gap. b) Valley polarization (VP), shown as color, and intervalley coherence (IVC) in the valley-filtered basis, shown with arrows, of the $\nu = +2$ CTI₁ state at $\Delta V = 20$ meV and $\epsilon_r = 16$ from 24×24 HF. Cyan (magenta) square denotes the Γ_M point of valley K (K') in b,c,d). c) The momentum-resolved overlap in valley K of the valley-filtered basis in b) and the single-particle conduction basis. We observe that in some regions, the overlap vanishes due to mixing with the single-particle valence band, allowing the Chern number of the valley-filtered bands to differ from the single-particle conduction bands. d) The direct band gap between the HF valence and conduction bands in valley K for a symmetry-preserving 16×16 HF calculation at $\nu = +2$. Comparing with c), we observe that band hybridization occurs where the energy difference is small. For b,c,d), we only show the quantities in one spin sector.

spectrum contains an isolated⁵ IVC band above or below E_F (within a spin sector), we can unfold this HF band $|\text{HF}, \mathbf{k}\rangle$ into two normalized valley-diagonal bands $|\text{HF}_+, \mathbf{k}\rangle$ and $|\text{HF}_-, \mathbf{k}\rangle$:

$$|\text{HF}, \mathbf{k}\rangle = \alpha(\mathbf{k}) |\text{HF}_+, \mathbf{k}\rangle + \beta(\mathbf{k}) |\text{HF}_-, \mathbf{k}\rangle. \quad (20)$$

For the IVC states in ABBA-stacked TDBG at $\nu = 2$, we define the valley-filtered basis using the unfilled HF band immediately above E_F in each spin sector, since it is isolated from the filled bands and higher remote conduction bands by charge gaps (the latter do not mix with the central bands in any significant way). We note that the valley-filtered basis for a CTI defined using Eq. 20 is ambiguous at discrete points in each valley where $|\text{HF}, \mathbf{k}\rangle$ is fully polarized into the other valley, but this

can be resolved by assuming that the valley-filtered basis is continuous in \mathbf{k} -space. We also comment that even though we extract the valley-filtered basis from an unfilled HF band, we continue to define the order parameter as $\Delta_{\mathbf{q}}(\mathbf{k}) \equiv \langle c_{\mathbf{k},+}^\dagger c_{\mathbf{k}+\mathbf{q},-} \rangle$, where $c_{\mathbf{k}\tau}^\dagger$ are *electron* creation operators for the valley-filtered basis⁶.

At $\Delta V = 20$ meV, the single-particle conduction band has Chern number $C = -2$ ($+2$) in valley K (K'), while the valence bands are trivial. For strong interactions, HF calculations at $\nu = +2$ find flavor-polarized insulators (Fig. 4). For weaker interactions, we find a \hat{T} and $SU(2)_s$ -symmetric IVC insulator⁷. However, the corresponding valley-filtered basis is found to have $C = +1$ (-1) in valley K (K'), which differs from that of the single-particle conduction bands, and the IVC order parameter winds by 4π instead of -8π around the mBZ (Fig. 3b). This means that we obtain a CTI₁, instead of a CTI₋₂ that would be naively expected by considering the non-interacting band topology. In Fig. 3c, we plot the overlap of the valley-filtered band with the single-particle conduction band, which vanishes at three \hat{C}_{3z} -related points in the mBZ. This allows the valley Chern number of the valley-filtered basis to differ from that of the single-particle conduction basis.

We note that the absolute value of the valley-filtered basis Chern number is lowered from 2 to 1. This is consistent with the notion that there is a tendency to reduce the winding (i.e. ‘unfrustrate’ the topological obstruction) of the order parameter, since this allows for more favorable exchange energetics. The system achieves this by substantially hybridizing with the single-particle valence band. Due to the kinetic energy penalty, such hybridization preferentially occurs at regions with small direct gap. We can roughly estimate the hybridization positions by performing symmetry-preserving HF at this filling, which partially accounts for interaction-induced renormalization effects (Fig. 3d). In this specific example, the hybridization occurs away from high symmetry points. This restricts the valley-filtered basis Chern number to change by multiples of 3 [85], which does not permit a full lifting of the topological frustration. For larger ΔV , we observe additional CTI _{n} phases, including two CTI₋₁ regions with distinct \mathbf{q} , highlighting the complex interplay between the kinetic energy and interaction effects.

We have also performed HF calculations at $\nu = 2$ for different twist angles θ to confirm that the CTI in ABBA-stacked TDBG is stable under a range of twist angles (Fig. 5).

⁵ We briefly discuss the situation where multiple HF bands are proximate in energy in Sec. III F.

⁶ The hole order parameter would differ by a minus sign.

⁷ Within spin-collinear HF calculations, states with different IVC angles in the two spin sectors are degenerate with $SU(2)_s$ -symmetric IVC states.

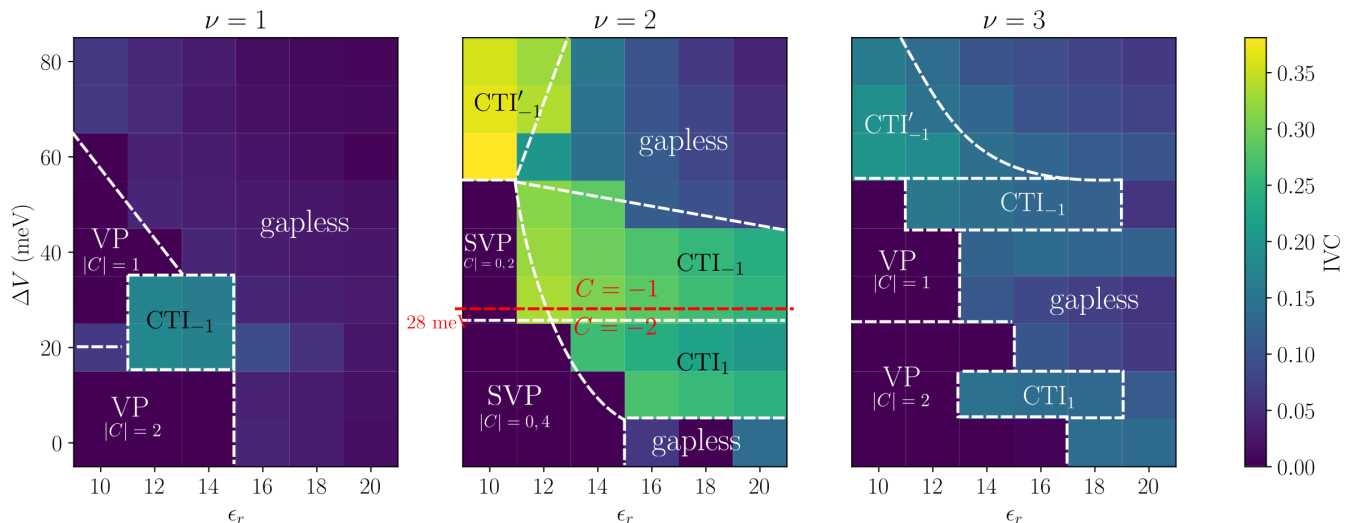


FIG. 4. **Phase diagram of ABBA-stacked twisted double-bilayer graphene (TDBG) at $\theta = 1.2^\circ$.** The results are obtained using 12×12 HF at $\nu = 1, 2, 3$. VP denotes valley-polarized states, which also carry a non-zero spin polarization. SVP denotes spin- or valley-polarized states, which are degenerate in HF. TVP denotes tilted-valley-polarized states. Topological transitions in the non-interacting band structure are marked in red, with the Chern number refers to that of the central conduction band. CTI' has a different intervalley spiral wavevector \mathbf{q} from the unprimed CTI states.

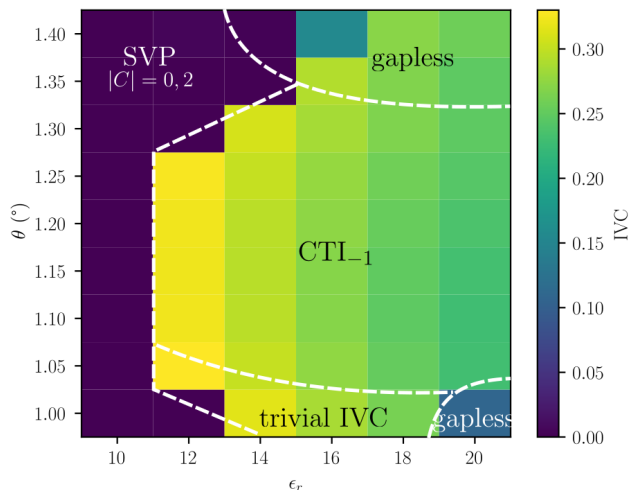


FIG. 5. **Phase diagram of ABBA-stacked twisted double-bilayer graphene (TDBG) with variable twist angle.** The results are obtained using 12×12 HF at $\nu = 2$ and $\Delta V = 40$ meV. SVP denotes spin- or valley-polarized states, which are degenerate in HF. We observe that the CTI is stable under a range of twist angles.

C. Twisted monolayer-bilayer graphene

Twisted monolayer-bilayer graphene (TMBG) is similar to ABAB-stacked TDBG in that it realizes an isolated conduction band with valley Chern number 2 at finite interlayer potential [45, 57] (Fig. 6). Its phase diagram is shown in Fig. 7. We find regions of CTI₂ at moderately high interlayer potential ΔV for $\nu = 1, 2$. At lower in-

terlayer potentials, we also find a trivial IVC insulator with TRS at $\nu = 2$, where ‘trivial’ means that the valley-filtered bands have vanishing Chern number (Fig. 6c). This allows the IVC to be non-vanishing across the mBZ. For such small ΔV , the non-interacting conduction and valence bands are not isolated (Fig. 6a), leading to strong inter-band hybridization which alleviates the IVC obstructions.

We stress that the IVC vortices discussed so far are momentum-space vortices, which are distinct from possible vortices in the real-space IVC order parameter. We define the latter as $\Delta_f(\mathbf{r}) = \langle \psi_{+,f}^\dagger(\mathbf{r}) \psi_{-,f}(\mathbf{r}) \rangle$, where $+, -$ are valley labels and f indexes other degrees of freedom such as sublattice or layer. For the trivial IVC state in TMBG, we consider the real-space order parameter on sublattice A of the top layer, and observe a vortex and anti-vortex within the moiré unit cell (Fig. 6d). Hence, we conclude that the presence or absence of real-space IVC vortices cannot be directly used to discriminate between a CTI and a trivial IVC state. However, detailed scanning of the intra-moiré cell IVC pattern is still invaluable in providing evidence for the existence of specific IVC states, as was done for the IKS in TBG in Ref. [26].

In Ref. [51], insulating states with vanishing Chern number $C = 0$ were experimentally observed in TMBG at $\nu = 1$ with finite displacement field in multiple devices with twist angles $\theta \simeq 1.1^\circ - 1.2^\circ$. Since a fully flavor polarized state would have non-zero Chern number due to the single-particle band structure, while the CTI states have zero Chern number, this indirectly supports a CTI state. The theoretically calculated valley magnon instability with finite momentum transfer in Ref. [51] is

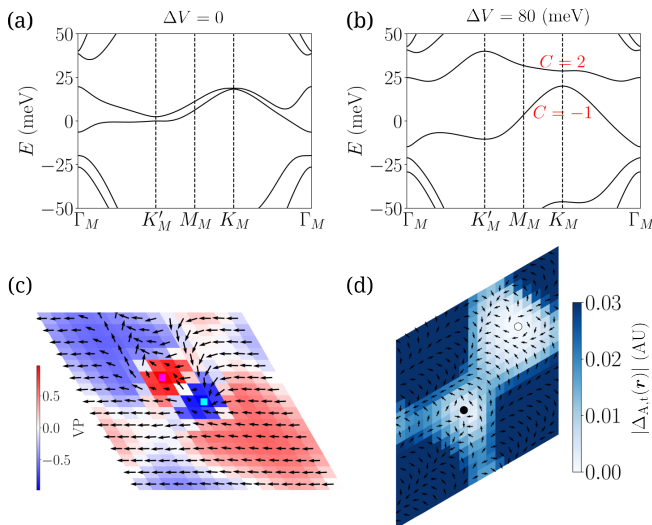


FIG. 6. **Twisted monolayer-bilayer graphene (TMBG) at $\theta = 1.2^\circ$.** a) Single-particle band structure at zero interlayer potential. The direct gap between the two central bands is nearly vanishing. b) At finite interlayer potential of $\Delta V = 80$ (meV), the conduction and valence bands are well-isolated with Chern numbers 2 and -1 respectively. c) The *momentum-space* valley polarization (VP), shown as color, and intervalley coherence (IVC) in the valley-filtered basis, shown with arrows, of the $\nu = +2$ trivial IVC state at $\Delta V = 0$ and $\epsilon_r = 12$ in 15×15 HF. Cyan (magenta) square denotes the Γ_M point of valley K (K'). d) The same state as in c), but showing the *real-space* IVC order parameter *within* a moiré unit cell for sublattice A on the top layer. The color shows the IVC magnitude and the arrows show the IVC phase angle, where we have subtracted off the spiral modulation due to finite \mathbf{q} . There is a vortex-antivortex pair, labelled with black and white circles. Note that the upper limit of the color scale has been clamped to show the regions near vortices more clearly.

also consistent with the finite- \mathbf{q} nature our proposed CTI state⁸.

D. Helical trilayer graphene

Helical trilayer graphene (HTG) is a super-moiré platform that hosts large-scale moiré-periodic domains whose isolated central bands carry strong-coupling valley Chern numbers of up to 2 [58–60, 86]. While HTG preserves \hat{C}_{2z} at the global scale, the domains (labelled h-HTG and h-TTG) individually break \hat{C}_{2z} . The presence of Kekulé spirals with a commensurate IVC wavevector \mathbf{q} was previously reported in HF studies at finite ΔV [61].

In Fig. 8, we show the phase diagram in the h-HTG domain of helical trilayer graphene at $\theta = 1.85^\circ$.

⁸ However, the authors of Ref. [51] conclude that the state breaks time-reversal symmetry, which differs from the CTI setting.

For strong interactions (small ϵ_r), we have the ‘strong-coupling’ phase which can be understood by fully occupying certain spin- and valley-diagonal Chern bands [61]. Near the phase boundary to the intermediate-coupling phases, there can be small amounts of IVC arising from momentum-local excitonic instabilities. For $\epsilon \sim 15$ and $\nu = +2$, we find three gapped IVC phases that preserve TRS. The two phases for small and large interlayer potential ΔV have trivial IVC, as diagnosed by the non-vanishing of IVC across the mBZ, and the fact that the valley-filtered basis has $C = 0$. For intermediate ΔV , we find a CTI₁ phase. For weaker interactions, HF yields gapless phases. We note that a CTI₂ can be obtained by applying an artificially large sublattice potential (projected to the central bands). This is because the Chern basis bands with predominant weight on sublattice B (A) have $|C| = 2$ ($|C| = 1$). Hence by applying a large enough sublattice potential, the B bands can be sufficiently separated from the A bands so as to prevent interaction-induced mixing, and allow a CTI₂ constructed from the B bands.

For $\nu = 3$, we find a much narrower CTI₁ region, while for $\nu = 1$, we do not find any CTIs. In Sec. A1, we compute the phase diagram for $\theta = 1.75^\circ$, which yields sizable TR-symmetric insulating IVC regions, but none corresponding to CTIs. We also consider the inclusion of momentum-dependent tunneling in the single-particle continuum model, which captures the particle-hole asymmetry observed in the experimental phase diagram [58]. Again, we do not find any CTIs, suggesting that such states may not be robustly present in HTG.

E. Twisted transition metal dichalcogenide homobilayers

Twisted homobilayers of hexagonal TMDs such as MoTe₂ and WSe₂ are also ideal platforms for realizing narrow topological time-reversed bands. Unlike graphene-based systems, they have strong spin-orbit coupling such that the low-energy bands are spin-valley-locked to be either $K \uparrow$ or $K' \downarrow$ [87]. Twisted bilayer MoTe₂ (t MoTe₂) has attracted considerable attention due to its displacement field-tuned [88] Chern insulator at $\nu = -1$, and correlated topological phases, including fractional Chern insulators, at various other fillings [9–12, 89].

We focus on $\theta = 3.4^\circ - 4.0^\circ$ t MoTe₂, where the lowest single-particle valence band has $C = +1$ (-1) in valley K (K') for small interlayer potentials ΔV as demonstrated with continuum model calculations (Fig. 9a). This raises the question of whether a CTI₁ is feasible at $\nu = -1$. We note that the highest valence band is separated from the next valence band with opposite Chern number by $\lesssim 10$ meV, and there is a topological phase transition that trivializes the highest valence band at around $\Delta V = 26$ meV. As shown in Fig. 9b, HF yields a valley-polarized Chern insulator at $\Delta V = 0$,

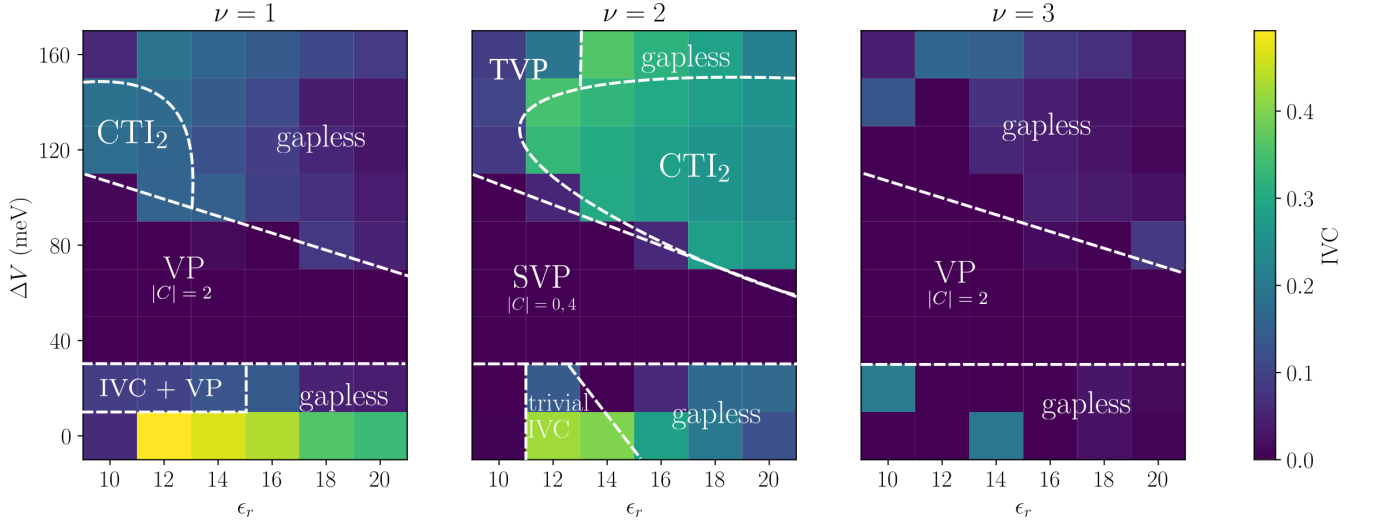


FIG. 7. **Phase diagram of twisted monolayer-bilayer graphene (TMBG) at $\theta = 1.2^\circ$.** The results are obtained using 12×12 HF at $\nu = 1, 2, 3$. VP denotes valley-polarized states, which also carry a non-zero spin polarization. SVP denotes spin- or valley-polarized states, which are degenerate in HF. TVP denotes tilted-valley-polarized states. IVC + VP denotes a state that is IVC in one spin sector and VP in the other spin sector.

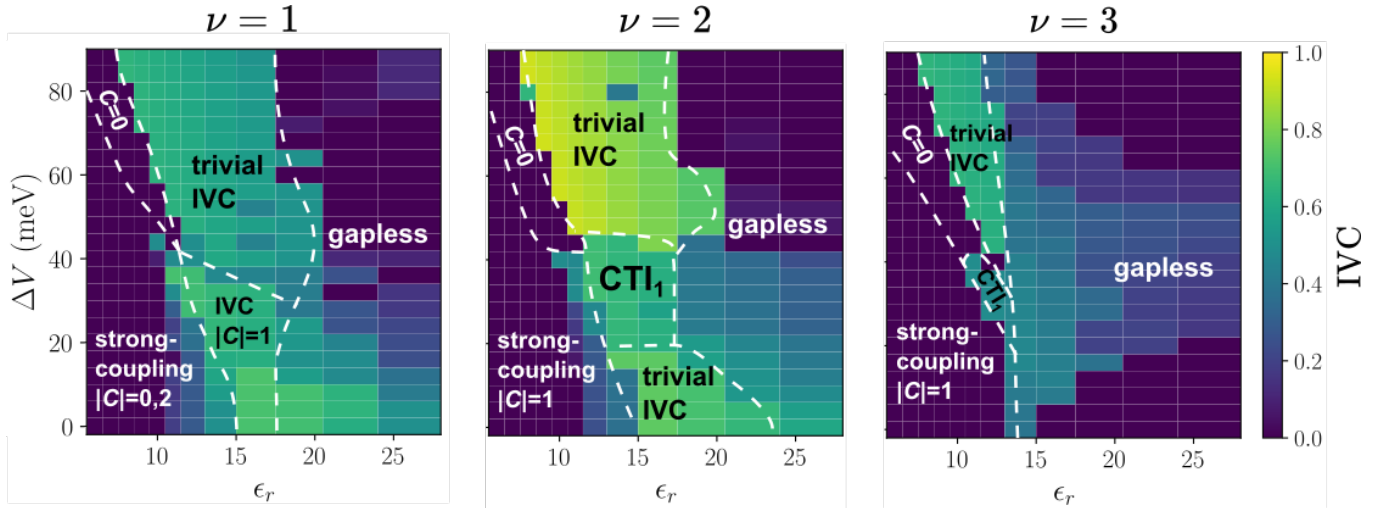


FIG. 8. **Phase diagram of helical trilayer graphene (HTG) at $\theta = 1.85^\circ$.** We focus on one h-HTG domain. Phase diagram calculated using 12×12 HF at $\nu = 1, 2, 3$. Momentum-dependent tunneling terms are not included.

while the ground state is a valley- and layer-polarized trivial insulator for strong interactions. For moderate interlayer potentials and weak/moderate interactions, we find a layer-polarized \hat{T} -symmetric⁹ IVC insulator [90]. However, this is not a CTI, as evidenced by the non-vanishing of IVC across the mBZ and the trivial valley-filtered Chern number of the unfilled HF band. While this is not surprising for large ΔV above the single-particle topological transition, the fact that this IVC

state remains unfrustrated for smaller $\Delta V < 26$ meV implies that interaction-induced hybridization with the next valence band removes the topological obstruction.

F. Twisted symmetric trilayer graphene

At the single-particle level, TSTG is \hat{C}_{2z} -symmetric, and at zero or low interlayer potential, the HF ground states preserve this symmetry. However, at large interlayer potential, Ref. 28 found a spontaneously \hat{C}_{2z} -breaking intervalley coherent state with non-zero intervalley boost vector \mathbf{q} , which is commensurate in the ab-

⁹ Our definition of \hat{T} for this subsection interchanges $(K \uparrow) \leftrightarrow (K' \downarrow)$ and satisfies $\hat{T}^2 = 1$.

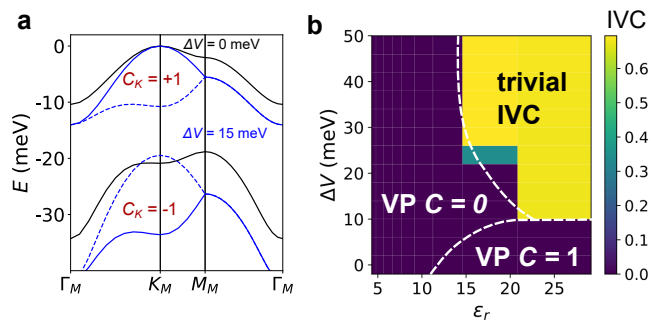


FIG. 9. **Twisted bilayer MoTe₂ at $\theta = 4^\circ$.** a) Single-particle valence band structure at $\Delta V = 0$ meV (black) and 15 meV (blue). Valley K (K') is shown with solid (dashed) lines. The band closest to charge neutrality has non-trivial valley Chern number for $\Delta V < 26$ meV. b) Phase diagram calculated using 12×12 HF at $\nu = -1$. VP indicates fully valley polarized (which also implies spin polarized due to spin-valley-locking). Trivial IVC denotes a $C = 0$ layer-polarized phase with no intervalley frustration. Similar results are obtained for $\theta = 3.4^\circ, 3.7^\circ$.

sence of strain. Fig. 10 shows the phase diagram of unstrained TSTG at $\nu = 2$ in the displacement field-interaction plane, with the commensurate Kekulé spiral region now characterized as ‘trivial IVC’, for reasons we now describe.

Characterizing possible intervalley frustration in the IVC phase is more nuanced in TSTG than in the other materials discussed so far. In the previous cases, for $\nu > 0$, there is only one empty band per spin sector that contains IVC (the higher remote bands do not qualitatively affect the physics), and the valley-filtered basis is naturally extracted from this band. In TSTG, since the single-particle band structure has no spectral gaps, there is no clear distinction between central and remote bands, and at the interacting level, there are multiple bands per spin sector both above and below the Fermi energy, many of which are not isolated. This makes the identification of a suitable valley-filtered basis difficult. Nevertheless, we find the *first* band above Fermi energy to be isolated, at least for some parameters, from which we can extract a valley-filtered basis. The corresponding intervalley order parameter is shown in Fig. 10a, which does not display winding of the IVC. As such, we conclude that the C_{2z} -breaking Kekulé spiral in TSTG is not a CTI.

IV. DISCUSSION

While we have investigated the HF phase diagrams for several moiré systems, as listed in Tab. I, the moiré paradigm offers near limitless combinations of constituent materials and tuning knobs that can generate favorable conditions for realizing textured excitonic states. So far, we have only uncovered CTIs in graphene-based platforms. Our calculations within a narrow twist an-

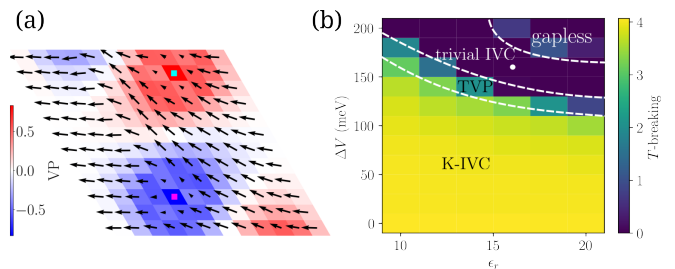


FIG. 10. **Twisted symmetric trilayer graphene (TSTG) at $\theta = 1.56^\circ$.** (a) The order parameter of the IVC state at $\Delta V = 160$ meV and $\epsilon_r = 16$, from 12×12 HF. The extraction of the basis is explained in the text. No intervalley frustration is observed, as evidenced by lack of full valley polarization anywhere in the mBZ and zero winding of the order parameter around the mBZ. (b) Phase diagram from 12×12 HF at $\nu = 2$. TVP denoted tilted valley polarized state. Besides the region labelled ‘gapless’, the K-IVC region is also not gapped.

gle range $\theta = 3.4^\circ - 4.0^\circ$ for twisted homobilayer MoTe₂ in Sec. III E have not yielded similar states. However, the single-particle models are known to vary significantly for different choices of TMDs and twist angles. For instance, for twisted bilayer WSe₂, as well as *t*MoTe₂ at smaller twist angles, density functional theory calculations have shown that the highest two valence moiré bands within a valley can have the same Chern numbers at zero displacement field [91]. This may influence the robustness of CTIs against trivialization of the intervalley coherence. Topological phases have also been experimentally observed in TMD heterobilayers [92]. Further exploration of the theoretical phase diagram is required to fully flesh out the nature of candidate IVC insulators in these TMD systems. Moiré platforms are natural potential hosts for CTIs because they often contain valleys which are mapped into each under time-reversal. More generally though, CTIs may arise as correlated insulators in other types of platforms if they are topological, are equipped with a time-reversal-odd $U(1)$ index, and exhibit competition between interactions and kinetic dispersion.

While we have found that several moiré materials favor the formation of CTIs in realistic parameter regimes, uncertainty in the modelling of the materials, in particular the effective interaction strength parameterized by ϵ_r , precludes more detailed predictions in the absence of specific experimental details. Other single-particle effects not treated here, such as strain (which is essential for the IKS, an example of an ETI in twisted bilayer and trilayer graphene [1]), would also impact the phase boundaries, including potentially widening the CTI regime. We also note that our calculations assume generalized translation symmetry on the moiré scale and hence ignores possible charge density wave (CDW) orders on this scale. Future work is required to establish the energetic competition of the CTI versus various moiré-scale density wave states.

CTIs are time-reversal invariant, meaning that, un-

like Chern insulators, they do not produce a quantized charge Hall response, which makes their experimental detection more challenging. In Ref. 51, the authors detected a $C = 0$ insulating state at $\nu = 1$ in TMBG at finite interlayer potential. Since valley polarized states are expected to carry non-zero Chern numbers due to the non-interacting band topology, this provides an indirect piece of evidence for the existence of the CTI here. We note that the authors found non-vanishing anomalous Hall response at finite doping away from $\nu = 1$. An important direction therefore is to theoretically investigate whether time-reversal symmetry is broken when CTIs are doped away from integer fillings (as was studied in Ref. [93] for the IKS in TBG, which is an ETI). In cases where time-reversal continues to be preserved, then the CTI may be a potential correlated insulating parent state that can be doped to yield superconductivity, although this seems to occur very rarely in \hat{C}_{2z} -breaking moiré platforms.

Due to their finite intervalley coherence, CTIs in moiré systems are expected to produce translation symmetry-breaking patterns on the *atomic* scale, such as $\sqrt{3} \times \sqrt{3}$ Kekulé charge patterns observed with scanning tunnelling microscopy in twisted graphene materials [26, 27, 94, 95]. Detection of such patterns provides supporting evidence for the existence of IVC which is necessary for CTIs. Furthermore, the spiral wavevector \mathbf{q} can be extracted from detailed analysis of the *moiré*-scale modulation of the IVC [26, 27], which can be compared with

theoretical predictions. We emphasize that, unlike the real-space IVC vortices detected in Ref. 26 *within* a moiré unit cell, the valley pseudospin texturing we have discussed for CTIs occurs in momentum space. As we have illustrated with an explicit example from TMBG, it is possible for a state without momentum space vortices (a ‘trivial IVC’ insulator by our criteria) to still carry vortices in the real-space IVC order parameter. Nevertheless, detailed real-space maps of the IVC texturing within a moiré cell can be fruitfully compared between experiment and theory to reinforce the interpretation of specific correlated states [26].

ACKNOWLEDGMENTS

We thank Jonah Herzog-Arbeitmann, Andrei Bernevig, and Jiabin Yu for useful discussions. This work was supported by a Leverhulme Trust International Professorship (Grant Number LIP-202-014, ZW), by a University of Zurich postdoc grant (FK-23-134, GW), by the European Research Council under the European Union Horizon 2020 Research and Innovation Programme via Grant Agreements No. 804213-TMCS (SAP) and No. 101076597-SIESS (NB), and by EPSRC Grants EP/S020527/1 and EP/X030881/1 (SHS). YHK is supported by a postdoctoral research fellowship at the Princeton Center for Theoretical Science.

-
- [1] Y. H. Kwan, Z. Wang, G. Wagner, S. H. Simon, S. A. Parameswaran, and N. Bultinck, Textured exciton insulators, same arXiv posting.
- [2] Y. Cao, V. Fatemi, S. Fang, K. Watanabe, T. Taniguchi, E. Kaxiras, and P. Jarillo-Herrero, Unconventional superconductivity in magic-angle graphene superlattices, *Nature* **556**, 43 (2018).
- [3] M. Yankowitz, S. Chen, H. Polshyn, Y. Zhang, K. Watanabe, T. Taniguchi, D. Graf, A. F. Young, and C. R. Dean, Tuning superconductivity in twisted bilayer graphene, *Science* **363**, 1059 (2019).
- [4] X. Lu, P. Stepanov, W. Yang, M. Xie, M. A. Aamir, I. Das, C. Urgell, K. Watanabe, T. Taniguchi, G. Zhang, A. Bachtold, A. H. MacDonald, and D. K. Efetov, Superconductors, orbital magnets and correlated states in magic-angle bilayer graphene, *Nature* **574**, 653 (2019).
- [5] J. M. Park, Y. Cao, K. Watanabe, T. Taniguchi, and P. Jarillo-Herrero, Tunable strongly coupled superconductivity in magic-angle twisted trilayer graphene, *Nature* **590**, 249 (2021).
- [6] Y. Cao, V. Fatemi, A. Demir, S. Fang, S. L. Tomarken, J. Y. Luo, J. D. Sanchez-Yamagishi, K. Watanabe, T. Taniguchi, E. Kaxiras, R. C. Ashoori, and P. Jarillo-Herrero, Correlated insulator behaviour at half-filling in magic-angle graphene superlattices, *Nature* **556**, 80 (2018).
- [7] A. L. Sharpe, E. J. Fox, A. W. Barnard, J. Finney, K. Watanabe, T. Taniguchi, M. A. Kastner, and D. Goldhaber-Gordon, Emergent ferromagnetism near three-quarters filling in twisted bilayer graphene, *Science* **365**, 605 (2019).
- [8] M. Serlin, C. L. Tschirhart, H. Polshyn, Y. Zhang, J. Zhu, K. Watanabe, T. Taniguchi, L. Balents, and A. F. Young, Intrinsic quantized anomalous hall effect in a moiré heterostructure, *Science* **367**, 900 (2020).
- [9] H. Park, J. Cai, E. Anderson, Y. Zhang, J. Zhu, X. Liu, C. Wang, W. Holtzmann, C. Hu, Z. Liu, T. Taniguchi, K. Watanabe, J.-H. Chu, T. Cao, L. Fu, W. Yao, C.-Z. Chang, D. Cobden, D. Xiao, and X. Xu, Observation of fractionally quantized anomalous hall effect, *Nature* **622**, 74 (2023).
- [10] J. Cai, E. Anderson, C. Wang, X. Zhang, X. Liu, W. Holtzmann, Y. Zhang, F. Fan, T. Taniguchi, K. Watanabe, Y. Ran, T. Cao, L. Fu, D. Xiao, W. Yao, and X. Xu, Signatures of fractional quantum anomalous hall states in twisted mote2, *Nature* **622**, 63 (2023).
- [11] Y. Zeng, Z. Xia, K. Kang, J. Zhu, P. Knüppel, C. Vaswani, K. Watanabe, T. Taniguchi, K. F. Mak, and J. Shan, Thermodynamic evidence of fractional chern insulator in moirémote2, *Nature* **622**, 69 (2023).
- [12] F. Xu, Z. Sun, T. Jia, C. Liu, C. Xu, C. Li, Y. Gu, K. Watanabe, T. Taniguchi, B. Tong, J. Jia, Z. Shi, S. Jiang, Y. Zhang, X. Liu, and T. Li, Observation of integer and fractional quantum anomalous hall effects in twisted bilayer mote2, *Phys. Rev. X* **13**, 031037 (2023).
- [13] Z. Lu, T. Han, Y. Yao, A. P. Reddy, J. Yang, J. Seo, K. Watanabe, T. Taniguchi, L. Fu, and L. Ju, Fractional quantum anomalous hall effect in a graphene moire su-

- perlattice (2023), [arXiv:2309.17436](https://arxiv.org/abs/2309.17436) [cond-mat.mes-hall].
- [14] Y. Xie, A. T. Pierce, J. M. Park, D. E. Parker, E. Khalaf, P. Ledwith, Y. Cao, S. H. Lee, S. Chen, P. R. Forrester, K. Watanabe, T. Taniguchi, A. Vishwanath, P. Jarillo-Herrero, and A. Yacoby, Fractional chern insulators in magic-angle twisted bilayer graphene, *Nature* **600**, 439 (2021).
- [15] A. Jaoui, I. Das, G. Di Battista, J. Díez-Mérida, X. Lu, K. Watanabe, T. Taniguchi, H. Ishizuka, L. Levitov, and D. K. Efetov, Quantum critical behaviour in magic-angle twisted bilayer graphene, *Nature Physics* **18**, 633 (2022).
- [16] H. Polshyn, M. Yankowitz, S. Chen, Y. Zhang, K. Watanabe, T. Taniguchi, C. R. Dean, and A. F. Young, Large linear-in-temperature resistivity in twisted bilayer graphene, *Nature Physics* **15**, 1011 (2019).
- [17] E. C. Regan, D. Wang, C. Jin, M. I. Bakti Utama, B. Gao, X. Wei, S. Zhao, W. Zhao, Z. Zhang, K. Yumigeta, M. Blei, J. D. Carlström, K. Watanabe, T. Taniguchi, S. Tongay, M. Crommie, A. Zettl, and F. Wang, Mott and generalized wigner crystal states in wse₂/ws₂ moiré superlattices, *Nature* **579**, 359 (2020).
- [18] J. M. Park, Y. Cao, L. Xia, S. Sun, K. Watanabe, T. Taniguchi, and P. Jarillo-Herrero, Magic-angle multilayer graphene: A robust family of moiré superconductors (2021), [arXiv:2112.10760](https://arxiv.org/abs/2112.10760) [cond-mat.supr-con].
- [19] Y. Zhang, R. Polski, C. Lewandowski, A. Thomson, Y. Peng, Y. Choi, H. Kim, K. Watanabe, T. Taniguchi, J. Alicea, *et al.*, Promotion of superconductivity in magic-angle graphene multilayers, *Science* **377**, 1538 (2022).
- [20] K. F. Mak and J. Shan, Semiconductor moiré materials, *Nature Nanotechnology* **17**, 686 (2022).
- [21] S. L. Sondhi, A. Karlhede, S. A. Kivelson, and E. H. Rezayi, Skyrmions and the crossover from the integer to fractional quantum hall effect at small zeeman energies, *Phys. Rev. B* **47**, 16419 (1993).
- [22] N. Bultinck, S. Chatterjee, and M. P. Zaletel, Mechanism for anomalous hall ferromagnetism in twisted bilayer graphene, *Phys. Rev. Lett.* **124**, 166601 (2020).
- [23] J. Ahn, S. Park, and B.-J. Yang, Failure of nielsen-ninomiya theorem and fragile topology in two-dimensional systems with space-time inversion symmetry: Application to twisted bilayer graphene at magic angle, *Phys. Rev. X* **9**, 021013 (2019).
- [24] Z. Song, Z. Wang, W. Shi, G. Li, C. Fang, and B. A. Bernevig, All magic angles in twisted bilayer graphene are topological, *Physical Review Letters* **123**, 10.1103/physrevlett.123.036401 (2019).
- [25] Y. H. Kwan, G. Wagner, T. Soejima, M. P. Zaletel, S. H. Simon, S. A. Parameswaran, and N. Bultinck, Kekulé spiral order at all nonzero integer fillings in twisted bilayer graphene, *Phys. Rev. X* **11**, 041063 (2021).
- [26] K. P. Nuckolls, R. L. Lee, M. Oh, D. Wong, T. Soejima, J. P. Hong, D. Călugăru, J. Herzog-Arbeitman, B. A. Bernevig, K. Watanabe, T. Taniguchi, N. Regnault, M. P. Zaletel, and A. Yazdani, Quantum textures of the many-body wavefunctions in magic-angle graphene, *Nature* **620**, 525 (2023).
- [27] H. Kim, Y. Choi, É. Lantagne-Hurtubise, C. Lewandowski, A. Thomson, L. Kong, H. Zhou, E. Baum, Y. Zhang, L. Holleis, *et al.*, Imaging intervalley coherent order in magic-angle twisted trilayer graphene, *Nature* **623**, 942 (2023).
- [28] Z. Wang, Y. H. Kwan, G. Wagner, N. Bultinck, S. H. Simon, and S. A. Parameswaran, Kekulé spirals and charge transfer cascades in twisted symmetric trilayer graphene, *Physical Review B* **109**, L201119 (2024).
- [29] Y.-H. Zhang, D. Mao, and T. Senthil, Twisted bilayer graphene aligned with hexagonal boron nitride: Anomalous hall effect and a lattice model, *Physical Review Research* **1**, 10.1103/physrevresearch.1.033126 (2019).
- [30] Y.-H. Zhang, D. Mao, Y. Cao, P. Jarillo-Herrero, and T. Senthil, Nearly flat chern bands in moiré superlattices, *Phys. Rev. B* **99**, 075127 (2019).
- [31] R. Bistritzer and A. H. MacDonald, Moiré bands in twisted double-layer graphene, *Proceedings of the National Academy of Sciences* **108**, 12233 (2011), <https://www.pnas.org/content/108/30/12233.full.pdf>.
- [32] G. W. Burg, J. Zhu, T. Taniguchi, K. Watanabe, A. H. MacDonald, and E. Tutuc, Correlated Insulating States in Twisted Double Bilayer Graphene, *Physical Review Letters* **123**, 197702 (2019).
- [33] Y. Cao, D. Rodan-Legrain, O. Rubies-Bigorda, J. M. Park, K. Watanabe, T. Taniguchi, and P. Jarillo-Herrero, Tunable correlated states and spin-polarized phases in twisted bilayer-bilayer graphene, *Nature* **583**, 215 (2020).
- [34] R. Du, J. Xiao, D. Zhang, X. Cai, S. Jiang, F. Lian, K. Watanabe, T. Taniguchi, L. Wang, and G. Yu, Ferromagnetism in twisted double bilayer graphene, *2D Materials* **11**, 025015 (2024), [arxiv:2404.18059](https://arxiv.org/abs/2404.18059) [cond-mat].
- [35] M. He, Y. Li, J. Cai, Y. Liu, K. Watanabe, T. Taniguchi, X. Xu, and M. Yankowitz, Symmetry breaking in twisted double bilayer graphene, *Nature Physics* **17**, 26 (2021).
- [36] L. Liu, S. Zhang, Y. Chu, C. Shen, Y. Huang, Y. Yuan, J. Tian, J. Tang, Y. Ji, R. Yang, K. Watanabe, T. Taniguchi, D. Shi, J. Liu, W. Yang, and G. Zhang, Isospin competitions and valley polarized correlated insulators in twisted double bilayer graphene, *Nature Communications* **13**, 3292 (2022).
- [37] X. Liu, Z. Hao, E. Khalaf, J. Y. Lee, Y. Ronen, H. Yoo, D. Haei Najafabadi, K. Watanabe, T. Taniguchi, A. Vishwanath, and P. Kim, Tunable spin-polarized correlated states in twisted double bilayer graphene, *Nature* **583**, 221 (2020).
- [38] P. Rickhaus, F. K. de Vries, J. Zhu, E. Portoles, G. Zheng, M. Masseroni, A. Kurzman, T. Taniguchi, K. Watanabe, A. H. MacDonald, T. Ihn, and K. Ensslin, Correlated electron-hole state in twisted double-bilayer graphene, *Science* **373**, 1257 (2021).
- [39] C. Rubio-Verdú, S. Turkel, Y. Song, L. Klebl, R. Samajdar, M. S. Scheurer, J. W. F. Venderbos, K. Watanabe, T. Taniguchi, H. Ochoa, L. Xian, D. M. Kennes, R. M. Fernandes, Á. Rubio, and A. N. Pasupathy, Moiré nematic phase in twisted double bilayer graphene, *Nature Physics* **18**, 196 (2022).
- [40] C. Shen, Y. Chu, Q. Wu, N. Li, S. Wang, Y. Zhao, J. Tang, J. Liu, J. Tian, K. Watanabe, T. Taniguchi, R. Yang, Z. Y. Meng, D. Shi, O. V. Yazyev, and G. Zhang, Correlated states in twisted double bilayer graphene, *Nature Physics* **16**, 520 (2020).
- [41] C. Zhang, T. Zhu, S. Kahn, S. Li, B. Yang, C. Herbig, X. Wu, H. Li, K. Watanabe, T. Taniguchi, S. Cabrini, A. Zettl, M. P. Zaletel, F. Wang, and M. F. Crommie, Visualizing delocalized correlated electronic states in twisted double bilayer graphene, *Nature Communications* **12**, 2516 (2021).

- [42] Y. Zhu, Y. Chen, Q. Li, Y. Chen, Y. Huang, W. Zhu, D. An, J. Song, Q. Gan, K. Wang, L. Wei, Q. Zong, K. Watanabe, T. Taniguchi, H. Wang, L. Huang, L. Xian, L. Sun, G. Yu, and L. Wang, Tunable multi-bands in twisted double bilayer graphene, *2D Materials* **9**, 034001 (2022).
- [43] M. He, J. Cai, Y.-H. Zhang, Y. Liu, Y. Li, T. Taniguchi, K. Watanabe, D. H. Cobden, M. Yankowitz, and X. Xu, Symmetry-Broken Chern Insulators in Twisted Double Bilayer Graphene, *Nano Letters* **23**, 11066 (2023).
- [44] M. Koshino, Band structure and topological properties of twisted double bilayer graphene, *Physical Review B* **99**, 235406 (2019).
- [45] J. Liu, Z. Ma, J. Gao, and X. Dai, Quantum Valley Hall Effect, Orbital Magnetism, and Anomalous Hall Effect in Twisted Multilayer Graphene Systems, *Physical Review X* **9**, 031021 (2019).
- [46] N. R. Chebrolu, B. L. Chittari, and J. Jung, Flat bands in twisted double bilayer graphene, *Physical Review B* **99**, 235417 (2019).
- [47] J. Y. Lee, E. Khalaf, S. Liu, X. Liu, Z. Hao, P. Kim, and A. Vishwanath, Theory of correlated insulating behaviour and spin-triplet superconductivity in twisted double bilayer graphene, *Nature Communications* **10**, 5333 (2019).
- [48] F. Haddadi, Q. Wu, A. J. Kruchkov, and O. V. Yazyev, Moiré Flat Bands in Twisted Double Bilayer Graphene, *Nano Letters* **20**, 2410 (2020).
- [49] J. Jung and A. H. MacDonald, Accurate tight-binding models for the π bands of bilayer graphene, *Physical Review B* **89**, 035405 (2014).
- [50] S. Chen, M. He, Y.-H. Zhang, V. Hsieh, Z. Fei, K. Watanabe, T. Taniguchi, D. H. Cobden, X. Xu, C. R. Dean, and M. Yankowitz, Electrically tunable correlated and topological states in twisted monolayer–bilayer graphene, *Nature Physics* **17**, 374 (2021).
- [51] M. He, Y.-H. Zhang, Y. Li, Z. Fei, K. Watanabe, T. Taniguchi, X. Xu, and M. Yankowitz, Competing correlated states and abundant orbital magnetism in twisted monolayer-bilayer graphene, *Nature Communications* **12**, 4727 (2021).
- [52] S.-y. Li, Z. Wang, Y. Xue, Y. Wang, S. Zhang, J. Liu, Z. Zhu, K. Watanabe, T. Taniguchi, H.-j. Gao, Y. Jiang, and J. Mao, Imaging topological and correlated insulating states in twisted monolayer-bilayer graphene, *Nature Communications* **13**, 4225 (2022).
- [53] H. Polshyn, J. Zhu, M. A. Kumar, Y. Zhang, F. Yang, C. L. Tschirhart, M. Serlin, K. Watanabe, T. Taniguchi, A. H. MacDonald, and A. F. Young, Electrical switching of magnetic order in an orbital Chern insulator, *Nature* **588**, 66 (2020).
- [54] H. Polshyn, Y. Zhang, M. A. Kumar, T. Soejima, P. Ledwith, K. Watanabe, T. Taniguchi, A. Vishwanath, M. P. Zaletel, and A. F. Young, Topological charge density waves at half-integer filling of a moiré superlattice, *Nature Physics* **18**, 42 (2022).
- [55] S. Xu, M. M. Al Ezzi, N. Balakrishnan, A. Garcia-Ruiz, B. Tsim, C. Mullan, J. Barrier, N. Xin, B. A. Piot, T. Taniguchi, K. Watanabe, A. Carvalho, A. Mishchenko, A. K. Geim, V. I. Fal’ko, S. Adam, A. H. C. Neto, K. S. Novoselov, and Y. Shi, Tunable van Hove singularities and correlated states in twisted monolayer–bilayer graphene, *Nature Physics* **17**, 619 (2021).
- [56] C. Zhang, T. Zhu, T. Soejima, S. Kahn, K. Watanabe, T. Taniguchi, A. Zettl, F. Wang, M. P. Zaletel, and M. F. Crommie, Local spectroscopy of a gate-switchable moiré quantum anomalous Hall insulator, *Nature Communications* **14**, 3595 (2023).
- [57] P. J. Ledwith, A. Vishwanath, and E. Khalaf, Family of Ideal Chern Flatbands with Arbitrary Chern Number in Chiral Twisted Graphene Multilayers, *Physical Review Letters* **128**, 176404 (2022).
- [58] L.-Q. Xia, S. C. de la Barrera, A. Uri, A. Sharpe, Y. H. Kwan, Z. Zhu, K. Watanabe, T. Taniguchi, D. Goldhaber-Gordon, L. Fu, T. Devakul, and P. Jarillo-Herrero, Helical trilayer graphene: a moiré platform for strongly-interacting topological bands (2023), [arXiv:2310.12204](https://arxiv.org/abs/2310.12204) [cond-mat.mes-hall].
- [59] T. Devakul, P. J. Ledwith, L.-Q. Xia, A. Uri, S. C. de la Barrera, P. Jarillo-Herrero, and L. Fu, Magic-angle helical trilayer graphene, *Science Advances* **9**, eadi6063 (2023), <https://www.science.org/doi/pdf/10.1126/sciadv.adi6063>.
- [60] N. Nakatsuji, T. Kawakami, and M. Koshino, Multiscale lattice relaxation in general twisted trilayer graphenes, *Phys. Rev. X* **13**, 041007 (2023).
- [61] Y. H. Kwan, P. J. Ledwith, C. F. B. Lo, and T. Devakul, Strong-coupling topological states and phase transitions in helical trilayer graphene, *Phys. Rev. B* **109**, 125141 (2024).
- [62] J. Yu, J. Herzog-Arbeitman, M. Wang, O. Vafek, B. A. Bernevig, and N. Regnault, Fractional chern insulators versus nonmagnetic states in twisted bilayer mote_2 , *Phys. Rev. B* **109**, 045147 (2024).
- [63] Y. Jia, J. Yu, J. Liu, J. Herzog-Arbeitman, Z. Qi, H. Pi, N. Regnault, H. Weng, B. A. Bernevig, and Q. Wu, Moiré fractional chern insulators. i. first-principles calculations and continuum models of twisted bilayer mote_2 , *Phys. Rev. B* **109**, 205121 (2024).
- [64] F. Wu, T. Lovorn, E. Tutuc, I. Martin, and A. H. MacDonald, Topological insulators in twisted transition metal dichalcogenide homobilayers, *Phys. Rev. Lett.* **122**, 086402 (2019).
- [65] C. Wang, X.-W. Zhang, X. Liu, Y. He, X. Xu, Y. Ran, T. Cao, and D. Xiao, Fractional chern insulator in twisted bilayer mote_2 , *Phys. Rev. Lett.* **132**, 036501 (2024).
- [66] A. P. Reddy, F. Alsallom, Y. Zhang, T. Devakul, and L. Fu, Fractional quantum anomalous hall states in twisted bilayer mote_2 and wse_2 , *Phys. Rev. B* **108**, 085117 (2023).
- [67] Y. Cao, J. M. Park, K. Watanabe, T. Taniguchi, and P. Jarillo-Herrero, Pauli-limit violation and re-entrant superconductivity in moiré graphene, *Nature* **595**, 526 (2021).
- [68] Z. Hao, A. M. Zimmerman, P. Ledwith, E. Khalaf, D. H. Najafabadi, K. Watanabe, T. Taniguchi, A. Vishwanath, and P. Kim, Electric field–tunable superconductivity in alternating-twist magic-angle trilayer graphene, *Science* **371**, 1133 (2021).
- [69] H. Kim, Y. Choi, C. Lewandowski, A. Thomson, Y. Zhang, R. Polski, K. Watanabe, T. Taniguchi, J. Alicea, and S. Nadj-Perge, Evidence for unconventional superconductivity in twisted trilayer graphene, *Nature* **606**, 494 (2022).
- [70] Y. Li, S. Zhang, F. Chen, L. Wei, Z. Zhang, H. Xiao, H. Gao, M. Chen, S. Liang, D. Pei, L. Xu, K. Watanabe, T. Taniguchi, L. Yang, F. Miao, J. Liu, B. Cheng, M. Wang, Y. Chen, and Z. Liu, Observation of Co-

- existing Dirac Bands and Moiré Flat Bands in Magic-Angle Twisted Trilayer Graphene, *Advanced Materials* **34**, 2205996 (2022).
- [71] J.-X. Lin, P. Siriviboon, H. D. Scammell, S. Liu, D. Rhodes, K. Watanabe, T. Taniguchi, J. Hone, M. S. Scheurer, and J. I. A. Li, Zero-field superconducting diode effect in small-twist-angle trilayer graphene, *Nature Physics* **18**, 1221 (2022).
- [72] X. Liu, N. J. Zhang, K. Watanabe, T. Taniguchi, and J. I. A. Li, Isospin order in superconducting magic-angle twisted trilayer graphene, *Nature Physics* **18**, 522 (2022).
- [73] C. Shen, P. J. Ledwith, K. Watanabe, T. Taniguchi, E. Khalaf, A. Vishwanath, and D. K. Efetov, Dirac spectroscopy of strongly correlated phases in twisted trilayer graphene, *Nature Materials* **22**, 316 (2022).
- [74] S. Turkel, J. Swann, Z. Zhu, M. Christos, K. Watanabe, T. Taniguchi, S. Sachdev, M. S. Scheurer, E. Kaxiras, C. R. Dean, and A. N. Pasupathy, Orderly disorder in magic-angle twisted trilayer graphene, *Science* **376**, 193 (2022), <https://www.science.org/doi/pdf/10.1126/science.abk1895>.
- [75] S.-J. Yang, J.-H. Jung, E. Lee, E. Han, M.-Y. Choi, D. Jung, S. Choi, J.-H. Park, D. Oh, S. Noh, K.-J. Kim, P. Y. Huang, C.-C. Hwang, and C.-J. Kim, Wafer-Scale Programmed Assembly of One-Atom-Thick Crystals, *Nano Letters* **22**, 1518 (2022).
- [76] N. J. Zhang, J.-X. Lin, D. V. Chichinadze, Y. Wang, K. Watanabe, T. Taniguchi, L. Fu, and J. I. A. Li, Angle-resolved transport non-reciprocity and spontaneous symmetry breaking in twisted trilayer graphene, *Nature Materials* **23**, 356 (2024).
- [77] X. Li, F. Wu, and A. H. MacDonald, *Electronic Structure of Single-Twist Trilayer Graphene* (2019), [arXiv:1907.12338 \[cond-mat\]](https://arxiv.org/abs/1907.12338).
- [78] E. Khalaf, A. J. Kruchkov, G. Tarnopolsky, and A. Vishwanath, Magic angle hierarchy in twisted graphene multilayers, *Physical Review B* **100**, 085109 (2019).
- [79] D. Calugaru, F. Xie, Z.-D. Song, B. Lian, N. Regnault, and B. A. Bernevig, Twisted symmetric trilayer graphene: Single-particle and many-body hamiltonians and hidden nonlocal symmetries of trilayer moiré systems with and without displacement field, *Phys. Rev. B* **103**, 195411 (2021).
- [80] J. Kang and O. Vafek, Strong coupling phases of partially filled twisted bilayer graphene narrow bands, *Phys. Rev. Lett.* **122**, 246401 (2019).
- [81] N. Bultinck, E. Khalaf, S. Liu, S. Chatterjee, A. Vishwanath, and M. P. Zaletel, Ground State and Hidden Symmetry of Magic-Angle Graphene at Even Integer Filling, *Phys. Rev. X* **10**, 031034 (2020), publisher: American Physical Society.
- [82] B. Lian, Z.-D. Song, N. Regnault, D. K. Efetov, A. Yazdani, and B. A. Bernevig, Twisted bilayer graphene. iv. exact insulator ground states and phase diagram, *Phys. Rev. B* **103**, 205414 (2021).
- [83] T. Wang, D. E. Parker, T. Soejima, J. Hauschild, S. Anand, N. Bultinck, and M. P. Zaletel, Kekulé spiral order in magic-angle graphene: a density matrix renormalization group study (2022), [arXiv:2211.02693 \[cond-mat.str-el\]](https://arxiv.org/abs/2211.02693).
- [84] Y.-H. Zhang, D. Mao, Y. Cao, P. Jarillo-Herrero, and T. Senthil, Nearly flat Chern bands in moiré superlattices, *Physical Review B* **99**, 075127 (2019).
- [85] C. Fang, M. J. Gilbert, and B. A. Bernevig, Bulk topological invariants in noninteracting point group symmetric insulators, *Physical Review B* **86**, 115112 (2012).
- [86] D. Guerci, Y. Mao, and C. Mora, Chern mosaic and ideal flat bands in equal-twist trilayer graphene (2023), [arXiv:2305.03702 \[cond-mat.mes-hall\]](https://arxiv.org/abs/2305.03702).
- [87] F. Wu, T. Lovorn, E. Tutuc, I. Martin, and A. H. MacDonald, Topological insulators in twisted transition metal dichalcogenide homobilayers, *Phys. Rev. Lett.* **122**, 086402 (2019).
- [88] E. Anderson, F.-R. Fan, J. Cai, W. Holtzmann, T. Taniguchi, K. Watanabe, D. Xiao, W. Yao, and X. Xu, Programming correlated magnetic states with gate-controlled moiré geometry, *Science* **381**, 325 (2023), <https://www.science.org/doi/pdf/10.1126/science.adg4268>.
- [89] K. Kang, B. Shen, Y. Qiu, K. Watanabe, T. Taniguchi, J. Shan, and K. F. Mak, Observation of the fractional quantum spin hall effect in moiré mote₂, *arXiv preprint arXiv:2402.03294* (2024).
- [90] T. Wang, T. Devakul, M. P. Zaletel, and L. Fu, Topological magnets and magnons in twisted bilayer mote₂ and wse₂ (2023), [arXiv:2306.02501 \[cond-mat.str-el\]](https://arxiv.org/abs/2306.02501).
- [91] X.-W. Zhang, C. Wang, X. Liu, Y. Fan, T. Cao, and D. Xiao, Polarization-driven band topology evolution in twisted mote₂ and wse₂ (2024), [arXiv:2311.12776 \[cond-mat.mtrl-sci\]](https://arxiv.org/abs/2311.12776).
- [92] T. Li, S. Jiang, B. Shen, Y. Zhang, L. Li, Z. Tao, T. Devakul, K. Watanabe, T. Taniguchi, L. Fu, *et al.*, Quantum anomalous hall effect from intertwined moiré bands, *Nature* **600**, 641 (2021).
- [93] G. Wagner, Y. H. Kwan, N. Bultinck, S. H. Simon, and S. A. Parameswaran, Global phase diagram of the normal state of twisted bilayer graphene, *Phys. Rev. Lett.* **128**, 156401 (2022).
- [94] D. Calugaru, N. Regnault, M. Oh, K. P. Nuckolls, D. Wong, R. L. Lee, A. Yazdani, O. Vafek, and B. A. Bernevig, Spectroscopy of twisted bilayer graphene correlated insulators, *Phys. Rev. Lett.* **129**, 117602 (2022).
- [95] J. P. Hong, T. Soejima, and M. P. Zaletel, Detecting symmetry breaking in magic angle graphene using scanning tunneling microscopy, *Phys. Rev. Lett.* **129**, 147001 (2022).

— Supplementary Material —

Appendix A: Additional numerical results

1. Helical trilayer graphene

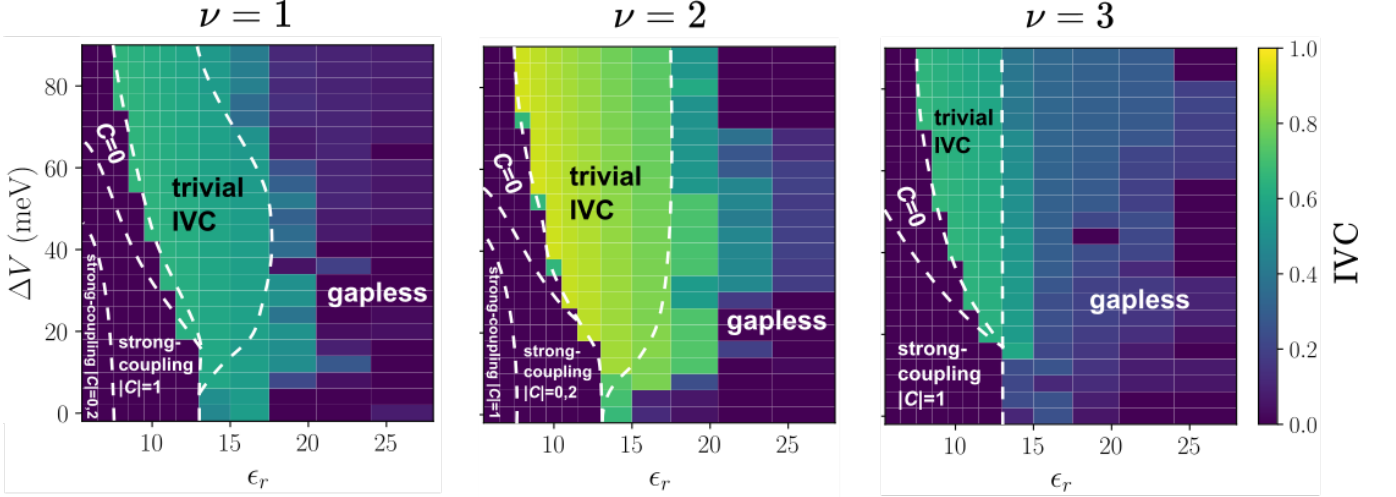


FIG. S1. Phase diagram of helical trilayer graphene (HTG) at $\theta = 1.75^\circ$. We focus on one h-HTG domain. Phase diagram calculated using 12×12 HF at $\nu = 1, 2, 3$. Momentum-dependent tunneling terms are not included.

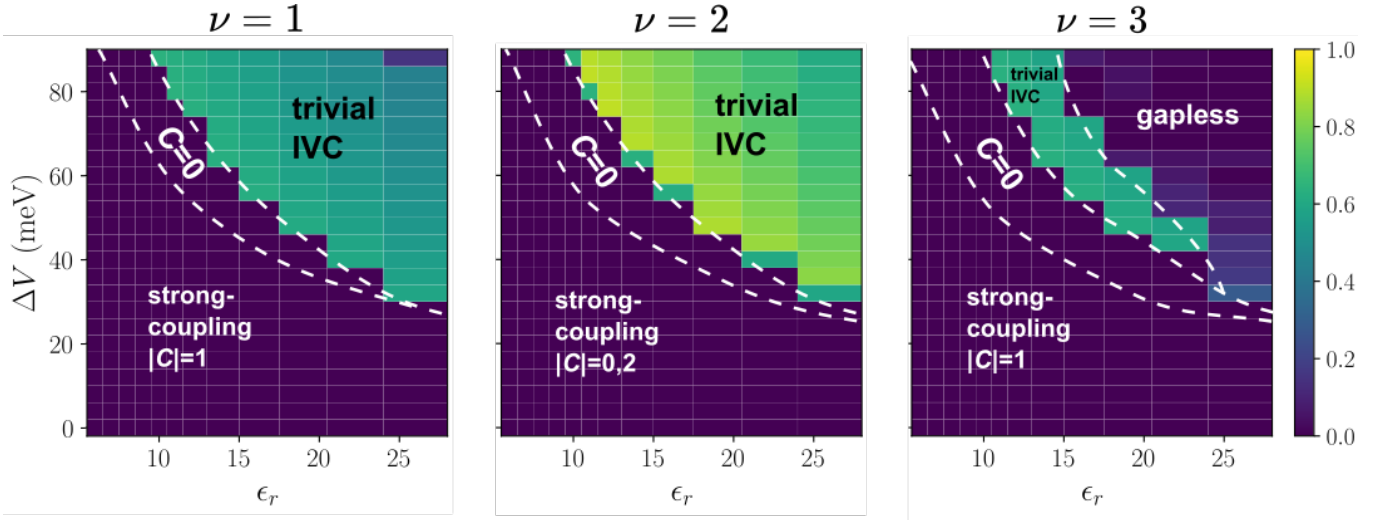


FIG. S2. Phase diagram of helical trilayer graphene (HTG) at $\theta = 1.85^\circ$ with momentum-dependent tunneling. We focus on one h-HTG domain. Phase diagram calculated using 12×12 HF at $\nu = 1, 2, 3$.

In Fig. S1, we show the phase diagram at $\nu = 1, 2, 3$ for the h-HTG domain of HTG at $\theta = 1.75^\circ$. While the overall structure of the competition between strong-coupling insulators at small ϵ_r , IVC states at intermediate ϵ_r , and gapless states at weak interactions is similar to that at $\theta = 1.85^\circ$ (shown in main text), we do not find any CTIs.

In Fig. S2, we show the phase diagram at $\nu = 1, 2, 3$ for the h-HTG domain of HTG at $\theta = 1.85^\circ$ when momentum-dependent interlayer tunneling is accounted for [58]. This introduces a momentum dependence to the interlayer hopping functions $t_\alpha(\mathbf{r})$ which varies linearly with the momentum deviation from the Dirac momentum. This enhances the strong-coupling phase at $\nu = 1, 2, 3$. We do not find any CTIs.

Appendix B: Gauge fixing and gauge-invariant velocity

1. Gauge fixing for intervalley order parameter

The intervalley order parameter $\Delta_{\mathbf{q}}(\mathbf{k}) \equiv \langle d_{\mathbf{k},+}^\dagger d_{\mathbf{k}+\mathbf{q},-} \rangle$ is dependent on the choice of gauge for the $d_{\mathbf{k}\tau}^\dagger$ operators. While many choices are possible, we require that the gauge is smooth within the BZ. That is, we require $|\langle u(\mathbf{k} + \delta\mathbf{k}) | u(\mathbf{k}) \rangle - 1| \rightarrow 0$ when $|\delta\mathbf{k}| \rightarrow 0$ for all \mathbf{k} , provided no BZ boundary is crossed, where $|u(\mathbf{k})\rangle$ is the periodic part of the Bloch wavefunction. Numerically, we carry out the procedure described below.

Consider an $N_1 \times N_2$ system. Denote $\mathbf{g}_i = \mathbf{G}_i/N_i$ for $i = 1, 2$, where \mathbf{G}_i is the i -th basis reciprocal lattice vector. Consider first the $\tau = +$ valley. Denote the crystal momentum $\tilde{\mathbf{k}} = \mathbf{k} - \tilde{\gamma} = m_1\mathbf{g}_1 + m_2\mathbf{g}_2$ as (m_1, m_2) , where the chosen reference point $\tilde{\gamma}$ needs not be Γ_M , and $0 \leq m_i \leq N_i - 1$. Starting from $(0, 0)$, we specify the gauge at $(m, 0)$ by demanding

$$\arg(\langle u(m_1 + 1, 0) | u(m_1, 0) \rangle) = 0 \quad (\text{B1})$$

for $m_1 = 0, \dots, N_1 - 2$. We then fix the gauge at all other points by demanding

$$\arg(\langle u(m_1, m_2 + 1) | u(m_1, m_2) \rangle) = 0 \quad (\text{B2})$$

for $m_1 = 0, \dots, N_1 - 1$ and $m_2 = 0, \dots, N_2 - 2$. This gauge is akin to the ‘Landau gauge’ for an arbitrary Chern band. For the $\tau = -$ valley, we perform the same procedure, except we define $\tilde{\mathbf{k}} = \mathbf{k} + \mathbf{q} - \tilde{\gamma} = m_1\mathbf{g}_1 + m_2\mathbf{g}_2$ to ensure the alignment of the BZ boundaries in both valleys.

2. Gauge-invariant velocity on a grid

The gauge invariant velocity on a continuous \mathbf{k} -space is defined in Eq. 19. For numerical calculation on a finite grid, we adopt the following definition

$$\mathbf{j}(\mathbf{k}) \cdot \delta\mathbf{k} = \arg \left(\frac{\Delta_{\mathbf{q}}(\mathbf{k} + \delta\mathbf{k})}{\Delta_{\mathbf{q}}(\mathbf{k})} \frac{\langle u_{\mathbf{k}+\delta\mathbf{k},+} | u_{\mathbf{k},+} \rangle}{\langle u_{\mathbf{k}+\mathbf{q}+\delta\mathbf{k},-} | u_{\mathbf{k}+\mathbf{q},-} \rangle} \right) \quad (\text{B3})$$

where the principal range is $\arg(x) \in [-\pi, \pi)$, as we expect $|\mathbf{j}(\mathbf{k}) \cdot \delta\mathbf{k}| \ll 1$ for a sufficiently fine momentum grid and not too close to the vortex core, where the velocity diverges. This definition reduces to the correct continuum limit by setting $|\delta\mathbf{k}| \rightarrow 0$ and has the advantage of being numerically reliable for arbitrarily non-smooth gauge choice.